Magnetostructural transition and magnetocaloric effect in MnNiGe$_{1.05}$ melt-spun ribbons

Gerardo Daniel-Pérez, J. L. Sánchez Llamazares, A. Quintana-Nedelcos, P. Álvarez-Alonso, R. Varga, and V. Chernenko

Articles you may be interested in

Giant magnetocaloric effect in isostructural MnNiGe-CoNiGe system by establishing a Curie-temperature window
Applied Physics Letters **102**, 122405 (2013); 10.1063/1.4798318

Magnetostructural phase transitions and magnetocaloric effects in MnNiGe$_{1-x}$Al$_x$
Applied Physics Letters **100**, 052404 (2012); 10.1063/1.3681798

Giant magnetocaloric effects by tailoring the phase transitions
Applied Physics Letters **96**, 172504 (2010); 10.1063/1.3399773

Magnetostructural phase transition and magnetocaloric effect in off-stoichiometric Mn$_{1.9-x}$Ni$_x$Ge alloys
Applied Physics Letters **93**, 122505 (2008); 10.1063/1.2990649

Magnetocaloric effect and magnetostructural coupling in Mn$_{0.92}$Fe$_{0.08}$CoGe compound
Journal of Applied Physics **117**, 17D103 (2015); 10.1063/1.4906437

Effects of the substitution of Al for Mn on structure, magnetic, and magnetocaloric properties in MnCoGe
Journal of Applied Physics **119**, 215104 (2016); 10.1063/1.4949492

Magnetostructural transition and magnetocaloric effect in MnNiGe$_{1.05}$ melt-spun ribbons

Gerardo Daniel-Pérez,[1,2] J. L. Sánchez Llamazares,[2,a)] A. Quintana-Nedelcos,[2]
P. Álvarez-Alonso,[3] R. Varga,[4] and V. Chernenko[5]
[1]*Instituto Tecnológico Superior de Irapuato (ITESI), 36821 Irapuato, Guanajuato, Mexico*
[2]*Instituto Potosino de Investigación Científica y Tecnológica, Camino a la Presa San José 2055 Col.
Lomas 4ª, San Luis Potosí, S.L.P. 78216, Mexico*
[3]*Departamento de Electricidad y Electrónica, UPV/EHU, Barrio Sarriena s/n,
48940 Leioa, Spain*
[4]*Institute of Physics, University Pavol Jozef Šafárik, Park Angelinum 9, 04154, Košice, Slovakia*
[5]*BC Materials & University of Basque Country, UPV/EHU, Bilbao 48080, Spain*

Alloy ribbons of nominal composition MnNiGe$_{1.05}$ were produced using the melt-spinning technique.
As-quenched (aq) polycrystalline ribbons are single-phase showing the hexagonal Ni$_2$In-type crystal
structure. After thermal annealing at 1148 K, the formation of the orthorhombic TiNiSi-type crystal
structure by martensitic transformation is favored. However, XRD patterns for different temperatures
indicate that the phase transition from hexagonal to orthorhombic structure is incomplete. The starting
and finishing temperatures for the direct and reverse martensitic transformation for aq (annealed)
samples determined by DSC were $M_S = 264$ (268) K $M_f = 235$ (255) K, $A_S = 259$ (266) K, and $A_f = 289$
(276) K. Across this structural phase transition the annealed sample undergoes a drop in magnetization
giving rise to a narrow temperature dependence of the magnetic entropy change with a peak value on
heating (cooling) of 5.8 (4.8) Jkg^{-1}K^{-1} for a field change of 5 T. © *2014 AIP Publishing LLC*.
[http://dx.doi.org/10.1063/1.4864435]

Materials exhibiting large (or giant) and tuneable magnetocaloric effect (MCE) around room temperature are currently of considerable interest due to their potential application as magnetic refrigerants.[1]

The stoichiometric bulk NiMnGe alloy crystallizes from the melt in a Ni$_2$In-type hexagonal structure ($P6_3/mmc$; hereafter referred as austenite).[2] After long-term thermal annealing at high temperatures, this phase transforms at 470 K to a low-temperature orthorhombic TiNiSi-type martensitic phase ($Pnma$).[2,3] The magnetic moments in this phase are localized in Mn atoms ($\sim 2.8\,\mu_B$).[3,6] The orthorhombic structure orders antiferromagnetically (AFM) with a simple spiral-type magnetic structure and Néel temperature T_N of 346 K.[4–6] The AFM spiral is a non-collinear magnetic structure; due to the large Mn-Mn interatomic distances instead of a direct exchange a super-exchange interaction through the Ge atoms has been suggested as the origin of the magnetic structure.[3,6] Since the first-order martensitic transformation occurs well above T_N, the field-induced magnetic entropy change ΔS_M associated with this transition is negligible. However, Zhang and co-workers demonstrated that the structural transition temperature can be largely decreased by introducing vacancies of transition-metal (TM) atoms.[7] In fact, they reported giant MCE in Mn$_{1.9-x}$Ni$_x$Ge (x = 0.85, 0.855).[7] With the introduction of TM vacancies a large jump in magnetization ΔM is obtained because the structural transition temperature decreases giving rise to a magnetostructural transformation between the AFM orthorhombic TiNiSi-type phase and a ferromagnetic (FM)

hexagonal Ni$_2$In-type phase. More recently, a large magnetocaloric response has been also reported in Mn$_{1-x}$Co$_x$NiGe,[8,9] MnNi$_{1-x}$Fe$_x$Ge,[10] and Mn$_{1-x}$Fe$_x$NiGe[10] alloys.

Rapid solidification by using the melt-spinning technique has been recently applied to produce different Mn-based crystalline alloys of current interest as magnetocaloric materials such as (MnFe)$_2$(PGe),[11] Ni-Mn-X Heusler alloys (X = Sn, In),[12] and MnCoGe.[13] It is an effective one-step process to obtain single-phase alloys in the as-solidified state after significantly shortened thermal annealing compared to their bulk counterpart.

In this contribution, we report on the synthesis of melt-spun alloy ribbons of the off-stoichiometric alloy MnNiGe$_{1.05}$. Samples were studied in aq state and after a thermal annealing at 1148 K. The structural and magnetic behaviour, as well as the martensitic transformation and the accompanying magnetocaloric response are reported.

Alloy ribbons with thicknesses of $\sim 40\,\mu$m [see Fig. 1(a)] and 1.5–2.0 mm in width, and 5–12 mm in length) were produced by melt spinning from arc melted bulk ingots of nominal composition MnNiGe$_{1.05}$. Mn losses during arc melting were compensated. Melt spun samples were obtained in a Bülher model SC melt spinning system under a pure Ar atmosphere at linear speed of the cooper wheel of 20 ms^{-1}. Some amounts of the as-spun ribbons were annealed at 1148 K for 4 h under high vacuum to promote the formation of the orthorhombic structure. Annealing was followed by water quenching. X-ray diffraction (XRD) patterns for ribbon samples were obtained with a Bruker AXS D8 Advance diffractometer using Cu-Kα radiation. Low-temperature XRD measurements were performed in

---

a)Author to whom correspondence should be addressed. Electronic mail:
jose.sanchez@ipicyt.edu.mx.

vacuum using a commercial cryostat. Microstructure and composition were determined using a FEI/Philips XL30 FEG ESEM equipped with an energy-dispersive analysis system (EDS). Differential scanning calorimetry (DSC) curves were measured in a TA Instruments model 200 calorimeter with a heating/cooling rate of 10 K/min. Temperature at which austenite starts and finishes its phase transition into martensite, and vice versa, will be referred as M_S, M_f, and A_S, A_f, respectively. They were estimated by simple extrapolation from the DSC curves. The thermal hysteresis of the transformation is calculated as $\Delta T = (A_f - M_S)$.

Magnetization measurements were performed on powdered samples using a Quantum Design PPMS® EverCool-I platform equipped with a vibrating sample magnetometer module. Field-heated (FH) and field-cooled (FC) magnetization versus temperature $M(T)$ curves were recorded under applied magnetic fields of 0.2 T and 5 T.

Figure 1(a) shows the SEM images of the typical fracture cross-section microstructure of aq ribbons. Ribbons are fully crystalline and tend to exhibit columnar-grain microstructure in which the longer axis of individual grains orients perpendicular to both ribbon surfaces. After annealing, Fig. 1(b) shows that a considerable grain growth occurs, giving rise to a well-formed columnar-like microstructure with grains

growing along the entire ribbon thickness. EDS average percentage content of the elements for aq (annealed) ribbons is: 31.7 at. % (32.7 at. %) for Mn, 32.5 at. % (32.2 at. %) for Ni, and 35.8 at. % (35.0 at. %) for Ge. The standard deviation was 0.3–0.5 at. %. Hence, the starting chemical composition was reasonably reproduced in the alloy ribbons.

The room-temperature powder XRD patterns for aq and annealed ribbons are depicted in Figs. 1(c) and 1(e), respectively. XRD patterns were refined using the FullProf analytical package.[14] At room temperature both samples are single-phase and exhibit a hexagonal Ni_2In-type structure with cell parameters a = 4.073(2) Å, and c = 5.417(1) Å, and a = 4.0747(8) Å, and c = 5.4152(8) Å, respectively. The XRD pattern measured for the aq sample at 215 K [Fig. 1(d)] has been also indexed on the basis of a hexagonal structure [a = 4.061(2) Å and c = 5.415(2) Å]. However, notice the appearance of low-intensity peaks at 2θ positions that can be indexed as the (211) and (301) XRD peaks of the orthorhombic structure (i.e., the higher intensity XRD peaks of this phase). The DSC scans of this sample, plotted in Fig. 2(a), also confirm the hexagonal-to-orthorhombic phase transition. This structural phase transition is characterized by a broad endothermic/exothermic DSC peaks with $M_S = 264$ K, $M_f = 235$ K, $A_S = 259$ K, $A_f = 289$ K, and $\Delta T = 25$ K.

Fig. 1(f) shows the XRD pattern of the annealed sample at 215 K. Notice that in the annealed sample the orthorhombic structure coexists with some amount of the high-
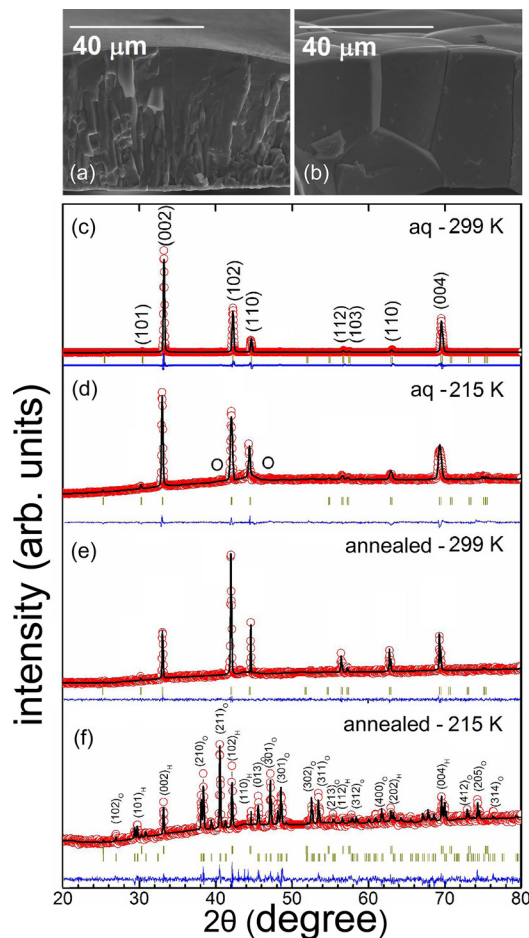

FIG. 1. (a) and (b) SEM images of the typical fracture cross-section microstructure of aq and annealed alloy ribbons, respectively. (c) and (d) XRD pattern at 299 K and 215 K for aq ribbons. The open circles indicate the (211) and (301) diffraction peaks of the orthorhombic phase. (e) and (f) XRD patterns at 299 K and 215 K for annealed ribbons.
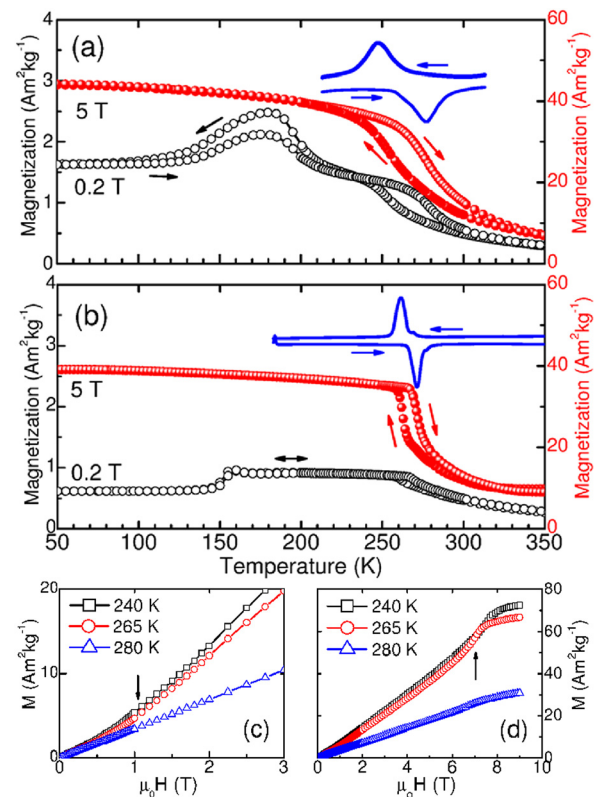

FIG. 2. FC and FH $M(T)$ curves at 0.2 T (scale: left Y-axis) and 5 T (scale: right Y-axis) and DSC scans for aq (a) and annealed (b) alloy ribbons. The heating or cooling paths of the curves are indicated by arrows. Isothermal magnetization curves measured at 240 K, 265 K and 280 K up to 9 T for annealed alloy ribbons: (c) zoom into the low-field region; (d) curves from 0 to 9 T. The vertical arrows roughly indicate the critical field at which the curves exhibit a change in the slope.

temperature hexagonal phase. The volume fraction of the orthorhombic phase estimated from the Rietveld refinement of the pattern was 82%. The calculated lattice parameters for the orthorhombic phase are a = 6.006(6) Å, b = 3.747(4) Å, and c = 7.042(9) Å, while those of the hexagonal one are a = 4.067(9) Å and c = 5.401(5) Å. The phase transformation is characterized by the following temperatures [the measured DSC curve is shown in Fig. 2(b)]: $M_S = 268$ K, $M_f = 255$ K, $A_S = 266$ K, $A_f = 276$ K, and $\Delta T = 12$ K. Hence, it occurs in a narrower temperature range in comparison with the one observed for aq samples. The structural transition temperatures determined are lower than those reported for MnNiGe$_{1.05}$ bulk polycrystalline alloys (i.e., $M_S = 297$ K, $M_f = 278$ K, $A_S = 285$ K, $A_f = 320$ K, and $\Delta T = 23$ K).[8] In Ref. 8, the authors estimated a Curie temperature for the hexagonal phase T_C^{hex} in this alloy of $\sim$205 K (it was obtained by simple extrapolation of the temperature dependence of the reciprocal magnetic susceptibility in the paramagnetic (PM) region). Following the same method we estimated for the annealed ribbon samples that T_C^{hex} is $\sim$248 K. This is important to know since it fixes the lower limit of temperature window in which the structural transition gives rise to a magnetostructural transition from a PM Ni$_2$In-type hexagonal phase to an AFM NiTiSi-type orthorhombic structure. The upper limit of the temperature window in which this coupled magnetostructural transition can occur is given by the Néel temperature T_N of the AFM orthorhombic phase. However, T_N is immeasurable since it is above the structural transition temperature. In order to prove the AFM character of the orthorhombic phase, we have measured the isothermal magnetization curves at 240 K, 265 K, and 280 K up to a maximum applied magnetic field $\mu_o H_{max}$ of 9 T. The low-field region and the curves up to 9 T are shown in Figures 2(c) and 2(d), respectively. At 240 K and 265 K the $M(\mu_o H)$ curves show a linear behavior with a change in the slope at a critical field of $\sim$1 T (indicated by a vertical arrow) that reveals the occurrence of a metamagnetic transition from a spiral AFM to a canted FM state, in accordance with the reported for the stoichiometric NiMnGe alloy.[3,15] Above a critical field of $\sim$ 7 T the canted FM state tends to saturate. In contrast, the $M(\mu_o H)$ curve at 280 K exhibits a linear paramagnetic behavior.

Figures 2(a) and 2(b) show the characteristic FC and FH $M(T)$ curves measured for aq and annealed ribbons, respectively. Arrows indicate whether the curve pathway corresponds to a heating or cooling regime. Notice that for both samples, the structural transition leads to a decrease in magnetization; nevertheless, it is more abrupt and therefore occurs in a narrower temperature range for the annealed one. The structural transition for the annealed samples occurs in a narrower temperature interval and shifts to higher temperature values, suggesting that a higher atomic ordering degree is reached upon annealing. In order to characterize the magnetocaloric effect linked to the AFM-PM phase transition, sets of isothermal magnetization curves were measured in the temperature range of the structural phase transition with a step increment of 1 K (up to a maximum applied magnetic field $\mu_o H_{max}$ of 5 T). The thermal protocol employed ensures that the phase transition is always crossed in the same direction (i.e., from austenite to martensite or vice versa). The inset of Fig. 3, shows the
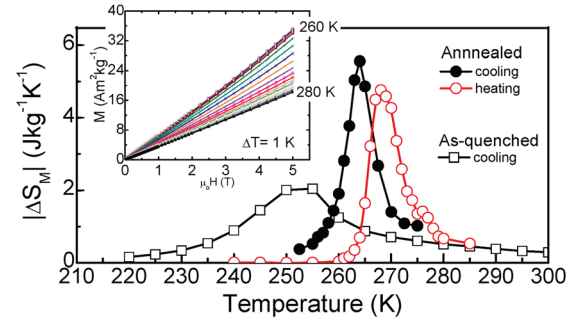

FIG. 3. ΔS_M(T) curves at $\mu_o \Delta H_{max} = 5$ T associated to the structural phase transition on cooling for the aq (open squares) and annealed (full circles) samples and on heating for the annealed samples (open circles). Inset: isothermal magnetization curves measured across the structural phase transition on heating.

typical set of magnetization isotherms measured across the structural transition. They are also reversible. The temperature dependence of the magnetic entropy change, $\Delta S_M(T)$, was obtained by numerical integration of the Maxwell relation $\Delta S_M(T) = \mu_0 \int_0^{\mu_0 H_{max}} \left(\frac{\partial M}{\partial T} \right)_{\mu_0 H} dH$. The curves obtained are shown in Fig. 3. The $\Delta S_M(T)$ curve for the aq sample shows a low peak value ΔS_M^{peak} of 2.0 Jkg^{-1}K^{-1} (absolute value) at 5 T located at $\sim$ 250 K. This agrees with the broader magnetization decay. For annealed ribbons larger values of ΔS_M^{peak} are obtained (i.e., between 5.8 and 4.8 Jkg^{-1}K^{-1} for the cooling and heating processes).

In summary, from the present study the following conclusions can be drawn: (a) as-solidified melt-spun ribbons of the ternary alloy MnNiGe$_{1.05}$ are single-phase exhibiting Ni$_2$In-type crystal structure; (b) ribbons exhibit a strongly ordered microstructure of columnar microcrystalline grains that grow with their longer axis aligned perpendicular to the ribbon plane; (c) the annealing time to produce the martensitic transformation from the hexagonal to the orthorhombic phase is considerably reduced in comparison with the one required for bulk alloys; and (d) the magneto-structural study indicates that the MCE in annealed ribbons is due to a coupled magnetostructural transition between a PM Ni$_2$In-type hexagonal phase to an AFM NiTiSi-type orthorhombic structure.

[1]O. Gutfleisch *et al.*, Adv. Mater. **23**, 821 (2011).
[2]V. Johnson, Inorg. Chem. **14**, 1117 (1975).
[3]W. Bażela *et al.*, Phys. Status Solidi A **38**, 721 (1976).
[4]H. Fjellvåg and A. F. Andresen, J. Magn. Magn. Mater. **50**, 291 (1985).
[5]A. Szytula *et al.*, Physica B & C **86–88**, 393 (1977).
[6]S. Nizioł *et al.*, J. Magn. Magn. Mater. **27**, 281 (1982).
[7]C. L. Zhang *et al.*, Appl. Phys. Lett. **93**, 122505 (2008).
[8]C. Zhang *et al.*, J. Phys. D: Appl. Phys. **43**, 205003 (2010).
[9]E. K. Liu *et al.*, Appl. Phys. Lett. **102**, 122405 (2013).
[10]E. Liu *et al.*, Nature Commun. **3**, 873 (2012).
[11]A. Yan *et al.*, J. Appl. Phys. **99**, 08K903 (2006).
[12]B. Hernando *et al.*, J. Magn. Magn. Mater. **321**, 763 (2009).
[13]C. F. Sánchez-Valdés *et al.*, Scripta Mater. **69**, 211 (2013).
[14]J. Rodríguez-Carvajal, Physica B **192**, 55 (1993).
[15]E. Liu *et al.*, IEEE Trans. Magn. **47**, 4041 (2011).